Determination of material properties by use of third-harmonic generation microscopy.

Schins, J.M.; Schrama, Th.; Squier, J.; Brakenhoff, G.J.; Müller, M.

DOI
10.1364/JOSAB.19.001627

Publication date
2002

Published in
Journal of the Optical Society of America B - Optical Physics

Determination of material properties by use of third-harmonic generation microscopy

J. M. Schins and T. Schrama

Swammerdam Institute for Life Sciences, University of Amsterdam, P.O. Box 94062, 1090 GB Amsterdam, The Netherlands

J. Squier

Department of Electrical and Computer Engineering, University of California, San Diego, Urey Hall Addition, MC0339, 9500 Gilman Drive, La Jolla, California 92093-0339

G. J. Brakenhoff and M. Müller

Swammerdam Institute for Life Sciences, University of Amsterdam, P.O. Box 94062, 1090 GB Amsterdam, The Netherlands

Received August 7, 2001

The fundamental features of third-harmonic generation microscopy are examined both theoretically and experimentally, and the technique is applied to the characterization of layered structures. Measurements and model calculations have been performed of the third-harmonic yield generated from homogeneous layers. Model calculations based on the paraxial approximation show good agreement with the experimental results, despite the conditions of high numerical aperture. The method proposed here allows for the determination of (i) the layer's third-order susceptibility relative to that of the substrate, (ii) its index of refraction at the third-harmonic frequency relative to that at the fundamental frequency, and (iii) its thickness and for the identification of a gradient region between two adjacent layers.

OCIS codes: 180.6900, 190.4410, 190.4160, 120.6710.

1. INTRODUCTION

Unlike second-order parametric processes such as second-harmonic generation, which vanish in isotropic media, third-harmonic generation (THG) can be obtained in practically all kinds of material as long as the materials are transparent at the wavelengths involved. However, under strong focusing conditions all the harmonic radiation produced before the focus is reabsorbed coherently behind the focus as a result of the Gouy phase shift. In practice, this effect limits significant THG to sample geometries with an interface between two bulk materials that differ in dispersion or in third-order susceptibility.

When the amplitude of the driving electric field has a Gaussian profile, the paraxial equations that describe THG can be solved analytically to a large extent. This analysis was first made by Ward and New,[1] who followed closely the analysis of second-harmonic generation by Kleinman *et al.*[2] Strictly speaking, this description is valid only for small and intermediate numerical apertures, and in that regime it has proved to describe the experimental results accurately.[3,4]

Under tight focusing conditions, THG has an inherent optical sectioning capability as a result of the signal's third-order power dependence on laser intensity. Indeed, the potential of THG for microscopic applications has been recognized.[5–7] The high sensitivity of THG microscopy to spatial variations in third-order susceptibility and in dispersion makes it complementary to the classic microscopic techniques, such as phase contrast and differential interference contrast microscopy, which are sensitive only to spatial variations in refractive index.

In this paper we explore the potential of THG microscopy for material characterization, and we study the conditions under which the paraxial equations may be used for the theoretical description. The sample geometry is chosen to be as simple as possible: just one or two flat interfaces between isotropic, homogeneous bulk materials. All experimental results presented here were obtained with such samples. We start out theoretically in Section 2, reviewing the physical mechanism and introducing the parameters involved. The paraxial equations are solved analytically for a Gaussian profile of the incident beam and numerically for an evenly illuminated objective pupil (hat profile). Numerical solutions are presented only when the Gaussian theory does not suffice.

2. THEORY

In this section we describe the theoretical procedure that we used to calculate the THG response under various focusing conditions and for various specimen configurations. The calculations are based on the paraxial wave equation with two kinds of initial intensity distribution: the theoretically easy, tractable Gaussian profile and the experimentally more realistic hat profile.

0740-3224/2002/071627-08$15.00

A. Gaussian Profile

In isotropic, nonmagnetic materials the paraxial wave equations[8] for the fundamental (ω_f) and the third-harmonic ($\omega_{\mathrm{th}} = 3\omega_f$) field envelopes $E_f(\mathbf{r})$ and $E_{\mathrm{th}}(\mathbf{r})$ propagating in the z direction take the simple form (Gaussian units)

$$\left(2ik_f\frac{\partial}{\partial z} + \frac{\partial^2}{\partial x^2} + \frac{\partial^2}{\partial y^2}\right)E_f(\mathbf{r}) = 0,$$

$$\left(2ik_{\mathrm{th}}\frac{\partial}{\partial z} + \frac{\partial^2}{\partial x^2} + \frac{\partial^2}{\partial y^2}\right)E_{\mathrm{th}}(\mathbf{r}) = -4\pi\left(\frac{\omega_{\mathrm{th}}}{c}\right)^2\chi^{(3)}E_f{}^3(\mathbf{r})\exp(i\Delta kz). \quad (1)$$

In Eqs. (1) the wave numbers are defined as

$$k_f = \frac{2\pi n(\omega_f)}{\lambda_f},$$

$$k_{\mathrm{th}} = \frac{2\pi n(\omega_{\mathrm{th}})}{\lambda_{\mathrm{th}}},$$

$$\Delta k = 3k_f - k_{\mathrm{th}} = \frac{6\pi\Delta n}{\lambda_f},$$

where $\Delta n = n(\omega_f) - n(\omega_{\mathrm{th}})$ and with vacuum wavelengths $\lambda_f = 2\pi c/\omega_f$ and $\lambda_{\mathrm{th}} = 2\pi c/\omega_{\mathrm{th}}$ for the fundamental and the third harmonic, respectively. Third-order susceptibility $\chi^{(3)}$ is shorthand notation for isotropic tensor element $\chi^{(3)}(\omega_{\mathrm{th}};\omega_f,\omega_f,\omega_f)$ that describes the THG response of the material. The total electric field $\mathbf{E}(\mathbf{r},t)$ is related to the field envelopes $E_{\mathrm{th}}(\mathbf{r})$ and $E_{\mathrm{th}}(\mathbf{r})$ as

$$\mathbf{E}(\mathbf{r},t) = \mathbf{e}_{xy}\{E_f(\mathbf{r})\exp[i(k_fz - \omega_ft)] + E_{\mathrm{th}}(\mathbf{r})\exp[i(k_{\mathrm{th}}z - \omega_{\mathrm{th}}t)] + \mathrm{c.c.}\}. \quad (2)$$

That is, all fields are linearly polarized ($\mathbf{e}_{xy}$) in the xy plane, with time-independent envelopes. In practice, such a description is applicable to time-dependent envelopes as well, and it holds for pulse durations as short as 100 light cycles (in our experiments we used a pulse duration of the order of 10^5 light cycles).

The paraxial equations are solved by

$$E_f(\mathbf{r}) = \eta A_f\exp\left(-\frac{\eta k_fr^2}{2z_{\mathrm{Rn}}}\right),$$

$$E_{\mathrm{th}}(\mathbf{r}) = \eta A_{\mathrm{th}}(z)\exp\left(-3\frac{\eta k_fr^2}{2z_{\mathrm{Rn}}}\right), \quad (3)$$

where

$$\eta(z) = \frac{1}{1 + iz/z_{\mathrm{Rn}}},$$

$$A_{\mathrm{th}}(z) = 2\pi i\omega_{\mathrm{th}}\chi^{(3)}A_f{}^3\frac{S(z)}{n_{\mathrm{th}}c},$$

$$S(z) = \int^z \eta^2(\xi)\exp(i\Delta k\xi)\mathrm{d}\xi. \quad (4)$$

Besides peak amplitude A_f (and a constant phase) the only free parameter in this solution is z_{Rn}. This parameter—the so-called Rayleigh length—determines the numerical aperture [NA $(=n\sin\alpha)$] through the relation $z_{\mathrm{Rn}} = 2/k_f\sin^2\alpha$ and is equal to half of the confocal parameter ($b = 2z_{\mathrm{Rn}}$).

We now briefly consider some general characteristics of THG based on Eqs. (1)–(4). Under strong focusing conditions the Gouy phase shift prevents THG in isotropic media when $\Delta k \leqslant 0$.[8] This is the result of destructive interference of the third-harmonic radiation produced before focus with that generated after the focus. Efficient THG—through (partially) constructive interference—occurs only in case of an interface that changes either the dispersion or the nonlinear susceptibility.

At focus ($z = 0$) one has $\eta(0) = 1$, and the radial intensity distribution of the fundamental has a width at a $1/e$ maximum of $2\sqrt{z_{\mathrm{Rn}}/k_f}$. The radial intensity distribution of the THG beam is $\sqrt{3}$ times smaller than that of the fundamental. Precisely on the axis of symmetry ($r = 0$) the axial dependence of the fundamental is given by $\eta(z)$, so the intensity has a Lorentzian profile with a full width at half-maximum (FWHM) equal to $2z_{\mathrm{Rn}}$. For the (hypothetical) case of constant amplitude $A_{\mathrm{th}}(z)$, the THG intensity profile is exactly equal to that of the fundamental.

Equations (4) yield explicit analytical results only in a reduced number of special cases. Here we mention two of these cases:

(i) A single interface medium–air transition with exact zero phase mismatch in the medium ($\Delta k = 0$). In this case the amplitude of the THG signal is determined by

$$|S(z_0)|^2 = \left|\int^{z_0}\eta^2(\xi)\mathrm{d}\xi\right|^2 = \frac{z_{\mathrm{Rn}}{}^2}{1 + (z_0/z_{\mathrm{Rn}})^2},$$

where z_0 is the optical distance between the interface and the beam waist. Consequently, the THG intensity has a FWHM of $2z_{\mathrm{Rn}}$, exactly like the fundamental beam itself.

(ii) A double interface air–medium–air transition, with a medium thickness Δz far below the excitation wavelength. Here the amplitude of the THG signal is determined by

$$|S(z_0)|^2 = \left|\eta^2(z_0)\exp(i\Delta kz_0)\int_{z_0}^{z_0+\Delta\zeta}\mathrm{d}\xi\right|^2 = \left[\frac{\Delta z}{1 + (z_0/z_{\mathrm{Rn}})^2}\right]^2,$$

where z_0 is the optical distance between the thin slab and the beam waist. Consequently the THG intensity has a FWHM of $1.28z_{\mathrm{Rn}}$, as was pointed out by Barad *et al.*[5]

In most realistic cases, however, the integral of Eqs. (4) cannot be calculated analytically. We have therefore calculated integral $S(z)$ of Eqs. (4) numerically for layered structures, with the interfaces oriented perpendicularly to the direction of light propagation. At each interface

we impose continuity of the phase difference between the third-order (material) polarization and the generated third-harmonic beam. Consequently, the phase of $S(z)$ needs to be corrected, at every interface, with a constant value:

$$\Delta\phi = \Delta k_1 n_1(\omega_f) z_{\mathrm{if}} - \Delta k_2 n_2(\omega_f) z_{\mathrm{if}}.$$

Here subscripts 1 and 2 refer to the layers, and z_{if} is the distance from the interface to the focal plane. Medium-dependent optical distance $n(\omega_f) z_{\mathrm{if}}$ reflects the medium-dependent curvature of the wave fronts, as can be determined from the analytical solutions [Eqs. (3)] to the paraxial equations: Electric field envelopes $E_f(\mathbf{r})$ and $E_{\mathrm{th}}(\mathbf{r})$ at $z = n(\omega_f) z_{\mathrm{if}}$ are both independent of $n(\omega_f)$, provided that the Rayleigh length in the medium scales as an optical distance, i.e., $z_{\mathrm{Rn}} = n(\omega_f) z_{R1}$, with $z_{R1} = \lambda_f / \pi NA^2$ the Rayleigh length in vacuum $[n(\omega_f) = 1]$.

The integral to be calculated for an arbitrary number of interfaces can now be generalized as follows:

$$S(z) = \sum_j \exp(i\Delta\phi_j) \int_{q_j}^{r_j} \mathrm{d}\xi \frac{\exp(i\Delta k_j \xi)}{(1 + i\xi/z_{R,j})^2}, \qquad (5)$$

where the z-dependent integration limits (q_j and r_j) and phases ($\Delta\phi_j$) are determined iteratively:

$$\frac{q_{j+1}}{n_{j+1}(\omega_f)} = \frac{r_j}{n_j(\omega_f)},$$

$$r_j - q_j = \text{layer thickness},$$

$$\Delta\phi_{j+1} - \Delta\phi_j = \Delta k_j r_j - \Delta k_{j+1} q_{j+1}.$$

Equation (5) can also be used for calculation of THG in the case of a transition gradient, from one layer to another, either in the refractive index or in the third-order susceptibility. We consider only the case in which the layer gradient is in the direction of light propagation. To simulate such a gradient we calculated integral S for a transition region divided into many subregions, each of numerical step-size thickness. Every subregion is considered homogeneous, with third-order susceptibility $\chi^{(3)}$ and wave-vector mismatch Δk such that the transition from one bulk material to the other occurs linearly over the transition region.

B. Non-Gaussian Profile

No analytical solution to coupled Eqs. (1) has been published, to our knowledge, for other than Gaussian beam profiles. In most experimental situations, especially when one is measuring with high-NA objectives, the objective apertures are overilluminated. In this case one can simulate the experimental results by assuming a flat intensity distribution over the objective aperture. Fraunhofer diffraction of a flat beam profile at a circular aperture (hat profile) yields a radial amplitude distribution at focus given by the well-known Airy function $J_1(\zeta)/\zeta$, where J_1 is the first-order Bessel function (of the first kind) and $\zeta = r/r_0$ is the radial distance expressed in units of $r_0 = \lambda f/2\pi a$, where a is the radius of the aperture and f is the focal distance.[9] To calculate the third-harmonic beam profile generated by a fundamental beam that has an Airy distribution at focus we discretized coupled Eqs. (1), using a space-marching Crank–Nicholson algorithm.[10] We verified that the algorithm yields the correct $\sin(\eta)/\eta$ dependence of the fundamental's amplitude along axis of propagation z, where $\eta = z/z_0$ is the axial distance expressed in units of $z_0 = 2\lambda f^2/\pi a^2$.[9] Because of the high spatial frequencies of the hat profile far from focus, we performed the calculation by starting off at the focus, using Airy function $J_1(\zeta)/\zeta$ as a radial profile.

The calculations show that the THG beam generated by a hat-profile fundamental beam approaches a Gaussian profile in the far field, with a FWHM equal to 0.30 $\pm$ 0.01 times the diameter of the input beam. For a Gaussian input beam profile, however, we calculated a ratio for the FWHM of the harmonic and the fundamental beams of 0.58 $\pm$ 0.01, which is in agreement with the analytical value $1/\sqrt{3}$ derived above.

3. RESULTS

A. Experimental Setup

The experimental setup is shown schematically in Fig. 1. An optical parametric amplifier (Coherent, Sunnyvale, Calif., Model OPA-400) provides tunable radiation over the range 950–2200 nm. At a repetition rate of 250 kHz, ~100-fs pulses are produced, with a typical power of ~60 nJ. In the experiments, neutral-density filters are used to reduce the power entering the objective to <10 nJ per pulse. The output of the parametric amplifier is upcollimated by a telescope, passes a variable aperture and two additional lenses, and is focused onto the sample by a high-NA microscope objective. The positions of the variable aperture and the two lenses are such that the aperture is imaged onto the entrance pupil of the excitation objective and the laser enters the objective as a parallel beam. The upcollimation of the laser beam ensures that the variable aperture is overfilled significantly at all settings, ensuring an approximately flat intensity profile across the entrance pupil. The fundamental and THG beams are collected by a second high-NA objective placed collinearly. A bandpass filter is used to block the funda-

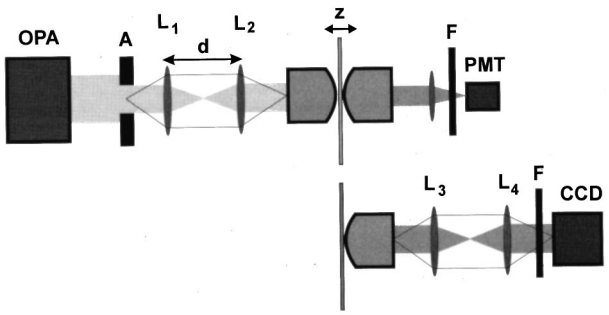

Fig. 1. Schematic of the experimental setup, with two variants for the detection path. An IR beam generated by the optical parametric amplifier (OPA) is apodized by a variable aperture (A) and imaged onto the entrance pupil of the excitation objective by means of two lenses (L_1 and L_2). L_2 and L_3 are the tube lenses of the respective microscope objectives. The distance between the two lenses (d) and the sample position (z) can be varied. The total amount of THG intensity is measured with a photomultiplier tube (PMT), with a filter (F) blocking out the fundamental. Alternatively, the numerical aperture of the THG signal is measured by imaging of the output pupil of the collection objective onto a CCD camera (CCD).

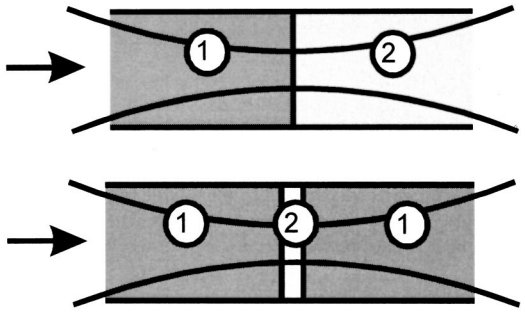

Fig. 2. Two sample geometries used in the experiments: top, with a single interface, also referred to as bulk–bulk, and bottom, with two interfaces, also referred to as bulk-layer–bulk. Media 1 and 2 are characterized by their refractive indices at the fundamental and tripled frequencies, $n(\omega_f)$ and $n(\omega_{\mathrm{th}})$, respectively, and by their third-order susceptibility $\chi^{(3)}$.

mental beam. The transmitted THG beam is detected by a photomultiplier tube. In one set of experiments the exit pupil of the collection objective was imaged onto a video camera (Hamamatsu Model C5985 CCD). This setting allowed for the measurement of the NA of the THG signal as a function of the excitation NA.

The focal position of the specimen is under piezoelectric control with position-sensor (Queensgate Model NS50 nanosensor) feedback, providing a positioning accuracy of 100 nm. The third-order power dependence of the third-harmonic signal on the input intensity has been checked regularly (results not shown). Also, spectral evaluation of the signal proved that no other than THG signals (e.g., white-light generation or fluorescence) were recorded.

In what follows we discriminate between basically two sample configurations. The single-interface configuration indicates an interface between two bulk media, each with its own dispersion characteristics and third-order nonlinear susceptibility. The second type of sample configuration is denoted a double interface. In this case there is a layer of a medium with different material properties inside a bulk medium. The two configurations are shown schematically in Fig. 2.

B. Single Interface

The microscope objectives are designed for roughly half of the wavelength that we used to excite the sample. Consequently, the optimal tube point position might be different from that specified by the manufacturer (Zeiss). We determined the optimal tube point position by measuring the total THG yield as a function of sample position z—denoted THG axial profiles in what follows—for several positions of lens L_1 relative to L_2. Figure 3(a) shows the THG axial profiles at three positions of L_1. Clearly the profile changes from broad and asymmetric for L_1 close to L_2 (335 mm), to narrow and symmetric (365 mm), and to broad and asymmetric again, though with opposite sign, for L_1 far from L_2 (405 mm). The FWHM, as well as the peak intensity, of the axial traces is plotted as a function of lens position in Fig. 3(b). The flip in asymmetry results from spherical aberration of the focused excitation beam. The lens position at which the THG yield culminates coincides with the absence of spherical aberration, which is clear evidence of diffraction-limited focusing. In spite of the quite different wavelengths used, the L_1–L_2 lens separation at which spherical aberration is canceled (365 ± 5 mm) coincides with the manufacturer's specifications (364.5 mm). This lens position was used in all further experiments reported here.

The width of the axial THG profiles determines the resolution of THG microscopy. Figure 4 shows how the width of the axial THG profiles depends on the excitation NA. Data were collected with two objectives: a 63 $\times$ 1.25-NA oil-immersion objective (open triangles) and a 40 $\times$ /0.65-NA air objective (filled circles). We adjusted the effective NA by changing the size of variable aperture A. With Φ_A the diameter of the variable aperture (as imaged onto the objective's entrance pupil), and Φ_{full} the objective's pupil diameter at full numerical aperture $\mathrm{NA}_{\mathrm{full}}$, the effective NA, $\mathrm{NA}_{\mathrm{eff}}$, follows from the ratio $\mathrm{NA}_{\mathrm{eff}}/\mathrm{NA}_{\mathrm{full}} = \Phi_A/\Phi_{\mathrm{full}}$. Pupil diameter Φ_{full} can be deduced from the objective's magnification M and tube length TL as $\Phi_{\mathrm{full}} = 2\mathrm{NA} \times \mathrm{TL}/M$. The correctness of this procedure has been demonstrated by experiments in

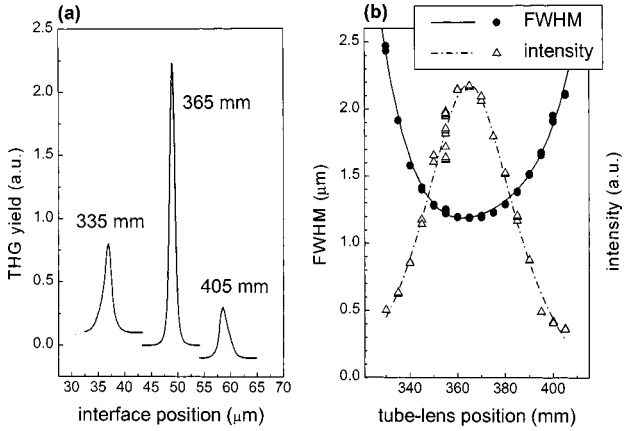

Fig. 3. THG dependence on tube-lens position for a glass–air interface, with 1.25-NA excitation at $\lambda_f = 1.2$ μm. (a) THG axial profiles measured at three tube lens positions. (b) FWHM and maximum THG intensity of the THG axial profile as a function of the tube-lens position. (The solid and dashed curves are guides to the eye only.)

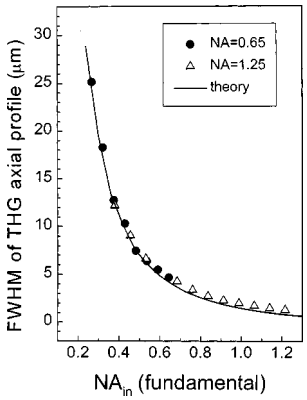

Fig. 4. FWHM of THG axial profiles from a glass–air interface as a function of input NA (fundamental). Solid line, prediction from Gaussian theory (no fitting parameters). The data represented by the filled circles were obtained with an air objective in the excitation path; the open triangles, with an oil-immersion objective.

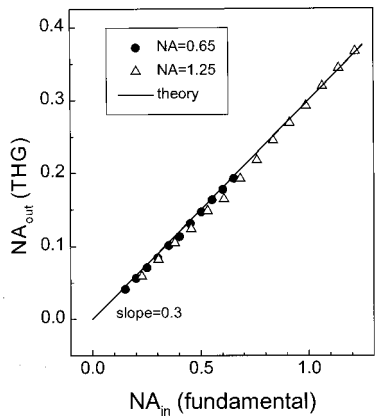

Fig. 5. Dependence of the output NA (THG) on the input NA (fundamental). Open triangles, data obtained with a 63 × / 1.25-NA (oil-immersion) objective; filled circles, with a 40 × / 0.65-NA (air) objective in the excitation path. The excitation beam approximately follows a radially flat intensity distribution (hat-profile excitation) at all input NA values.

which anomalous behavior was observed for $NA_{eff} > NA_{full}$.

We have found experimentally that the width of the THG axial profile decreases with increasing input NA, closely following an inverse square dependence. In Subsection 3.A we showed that, for $\Delta n = 0$, Gaussian theory predicts a Lorentzian axial profile for the THG signal, with a width equal to the confocal parameter of the excitation beam. We calculated the S integral [Eqs. (4)] numerically, for the experimental case of $\Delta n = -0.032$ (K5 glass with vacuum wavelengths of 1.2 μm and 400 nm for the fundamental and the THG beams, respectively). The numerical results are shown in Fig. 4 by the solid curve. There is excellent agreement between the experimental data and Gaussian theory for low NA, with a slight overestimate at high NA.

To measure the dependence of the output NA (THG) on the input NA (fundamental) we imaged the exit pupil of the collection objective onto a CCD camera. For all NAs the illumination distribution is close to a hat profile (flat intensity distribution with a hard, circular top), whereas the third-harmonic intensity profile is close to Gaussian. Excitation NA_{in} is calculated as indicated above. NA_{out} of the THG signal is determined as follows: The intensity profile at the exit pupil is fitted to a two-dimensional Gaussian with a single radius. We used the FWHM of the distribution determined from the fit to calculate the output NA according to $NA_{out} = FWHM \times NA_{full}/\phi_{full}$, where again ϕ_{full} and NA_{full} denote, respectively, the pupil diameter and full the NA of the collecting microscope objective. Figure 5 shows the results of this measurement. The output NA is equal to 0.3 ($\pm$0.01) times the input NA.

The solid curve in Fig. 5 represents the numerical results for hat-profile excitation. Because a radial hat profile in the far field corresponds to an Airy profile at focus, we obtained the numerical results by propagating an Airy function through the glass, as explained in Section 2. The theoretical slope is in excellent agreement with theory. This means that the paraxial model, which is valid in principle for small slope angles only, describes the higher-NA case just as well. It was found both experimentally and theoretically that the intensity distribution of the output THG beam always follows a Gaussian profile, even for the highest-NA hat-profile excitation. This suggests that the characteristics of the THG process are determined almost completely by the central—and highest-intensity—part of the focal region. This is in agreement with the third-order nonlinear nature of THG, considering that the largest differences between the focal field distributions produced by Gaussian- or hat-profile illumination of the pupil are found in the low-intensity wings of the distribution, which make a negligible contribution to the total THG yield.

The paraxial Gaussian theory[8] predicts a $1/\sqrt{3}$ ratio between the FWHM of the THG intensity distribution and that of the IR excitation intensity distribution. Instead, with a hat-profile excitation intensity distribution, this ratio becomes 0.3 if the THG output NA is defined again through the FWHM of the THG intensity distribution (as is done in this paper). It should be noted that other slope values are obtained when the width of the output THG intensity profile is defined differently. For example, the slope equals $1/\sqrt{3}$ when the Gaussian width is defined to be 7.5% of maximum intensity instead of half-maximum.

An important difference between Gaussian- and hat-profile excitation is in the functional form of the total THG yield as a function of axial position. In Subsection 3.A we showed that for $\Delta n = 0$ this profile is Lorentzian. Our calculations (results not shown) indicate that the axial THG profile is extremely close to Gaussian when the radial excitation profile is hatlike in the far field.

C. Two Interfaces

We now turn to a sample with two interfaces spaced approximately 10 μm apart. The two interfaces are resolved independently if the width of the focused axial intensity profile is much smaller than this separation. In this case, one expects two THG peaks as a function of sample position z (shown in Fig. 1), as in the situation when the beam focus lies exactly upon an interface. The specific sample geometry becomes important when the width of the axial intensity profile is of the order of, or slightly exceeds, the interface separation: Depending on the value of Δn in the gap (between the interfaces) the signal generation after the gap may interfere more positively or negatively with what was generated before the gap. Typical traces are presented in Fig. 6. To characterize the functional shape of the THG axial profile in this case we chose a limited number of parameters, as follows: With the first interface located at $z = 0$ and the second interface at $z = L$ we define three intensity ratios:

$$R_{pre} = \frac{I_{THG}(-L/4)}{I_{THG}(0)},$$

$$R_{post} = \frac{I_{THG}(+L/4)}{L_{THG}(0)},$$

$$R_{mid} = \frac{I_{THG}(+L/2)}{I_{THG}(0)}.$$

The THG yield is represented by I_{THG}, with the z position of the interface as its argument: The ratios represent the THG intensities that result when the focus lies exactly halfway between the interfaces, $I_{THG}(+L/2)$; one-quarter

gap thickness before the first interface, $I_{\mathrm{THG}}(-L/4)$; and likewise behind the first interface, $I_{\mathrm{THG}}(+L/4)$; all normalized by the intensity at the first interface, $I_{\mathrm{THG}}(0)$. The three relevant intensities are indicated in Fig. 6.

Model calculations of the behavior of the intensity ratios as a function of NA are presented in Fig. 7 (right-hand side) for an air-filled and an immersion-oil-filled gap

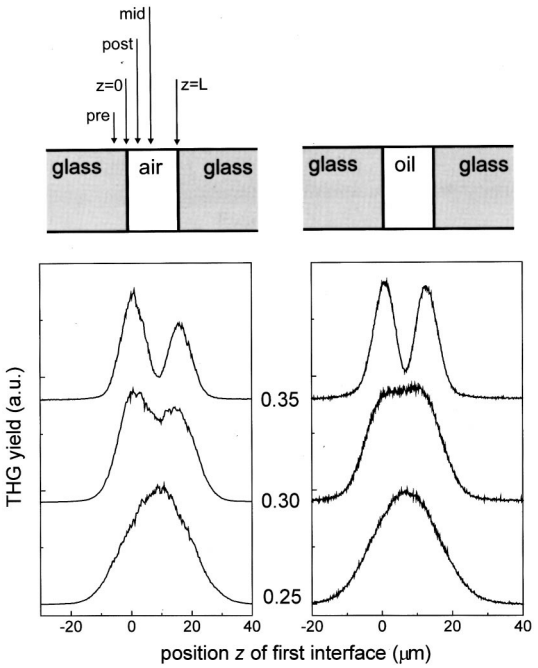

Fig. 6. Typical THG axial profiles for the double-interface configuration with either an air gap (left) or an immersion-oil gap (right). The gap is 8 μm thick and is situated between two K5 glass slides. The axial profiles are recorded at different input NA values of 0.25, 0.30, and 0.35 as indicated.

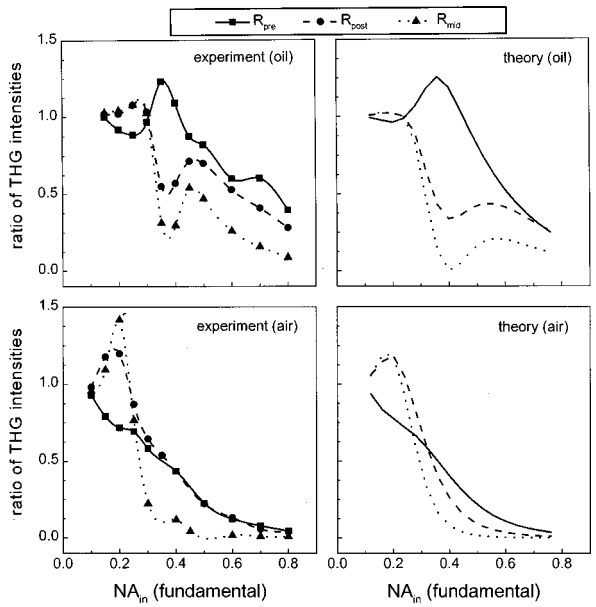

Fig. 7. Measured (left) and calculated (right) intensity ratios R_{pre}, R_{mid}, and R_{post} for a double-interface geometry. Gaps are filled with immersion oil or air, as shown. Experimental conditions are given in the text.

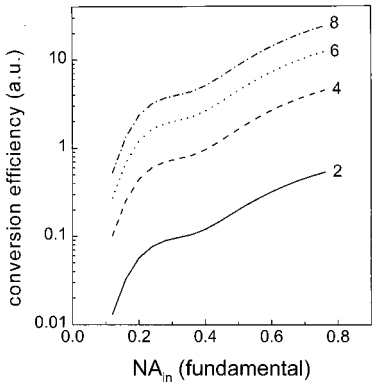

Fig. 8. Calculated THG conversion efficiencies as a function of NA of the excitation beam for four values of the third-order susceptibility ratio $\chi^{(3)}_{\mathrm{gap}}/\chi^{(3)}_{\mathrm{glass}}$. For all traces, $\Delta n_{\mathrm{gap}} = -0.022$ and $\Delta n_{\mathrm{glass}} = -0.032$.

between K5 glass slides. For comparison, the experimental data are displayed on the left-hand side in Fig. 7. Because the calculations were made for Gaussian beams, and the experiments were performed with hat-profile beams, the agreement is only qualitative. Nevertheless, the calculations reproduce the basic features of the experimental data. For the calculations we used $\Delta n_{\mathrm{oil}} = -0.028$ and $\Delta n_{\mathrm{K5}} = -0.032$, with $n_{\mathrm{oil}} = 1.50276$ and $n_{\mathrm{K5}} = 1.51146$ at $\lambda_{\mathrm{f}} = 1100$ nm. The ratio of the nonlinear susceptibilities of K5 glass and immersion oil was chosen arbitrarily to be $\chi^{(3)}_{\mathrm{oil}}/\chi^{(3)}_{\mathrm{K5}} = 3$. The numerical calculations show that the functional form of the signal depends almost solely on the change in refractive indices, whereas the magnitude of the THG signal depends primarily on the ratio of nonlinear susceptibilities (see the discussion below).

Figure 8 shows the strong dependence of the THG conversion efficiency (with the interface positioned at $z = 0$ μm) on susceptibility ratio $\chi^{(3)}_{\mathrm{gap}}/\chi^{(3)}_{\mathrm{glass}}$ as a function of NA. The THG conversion efficiency—i.e., the ratio between THG output power and IR input power (which is of the order of 10^{-7}–10^{-8} for glass–air interfaces[11])—is proportional to $|S/z_{\mathrm{Rn}}|^2$, where S is the integral of Eqs. (4). Because the absolute conversion efficiency of THG depends on the intensity of the fundamental beam, which for a given power depends on its pulse duration, we did not represent the results of our calculation in terms of absolute efficiencies. Note that the functional form of the THG conversion efficiency as a function of NA is almost independent of Δn_{gap} (data not shown).

D. Periodic Structures and Gradients

For periodic structures and gradients the S integral of Eqs. (4) must be generalized to Eq. (5). We performed some calculations that are relevant for the THG characterization of multilayer coatings. For example, one may wish to measure the thickness of deposited layers. Calculations point out that the visibility of a periodic stack of layers depends critically on layer thickness and dispersion. Figure 9 shows the visibility of 0.5-μm-thick layers scanned axially with a 1.0-NA IR beam of 1.55-μm wavelength. The visibility is defined as $|\log(Q)|$, where Q is

the ratio of THG yield with the IR focus exactly on the interface to that which is halfway between interfaces (Fig. 9, inset).

Whether THG microscopy can discriminate between a sudden and a gradual change of material parameters at an interface depends critically on the steepness of the gradient relative to the confocal parameter of the focused fundamental beam. Only when the zone of gradual change in material properties exceeds the confocal parameter can THG be used to characterize this gradient. For Fig. 10 two typical cases have been calculated: the dispersion of the two pure materials differs but not their third-order susceptibility (dashed curve) and the third-order susceptibility of the two pure materials differs but not their dispersion (solid curve). That for a sudden transition, i.e., in the limit of an infinitely steep gradient, these two curves do not converge is a property that is inherent in the process of THG buildup: Susceptibility transitions yield smaller THG axial profile widths (i.e., better resolution) than do dispersion transitions.

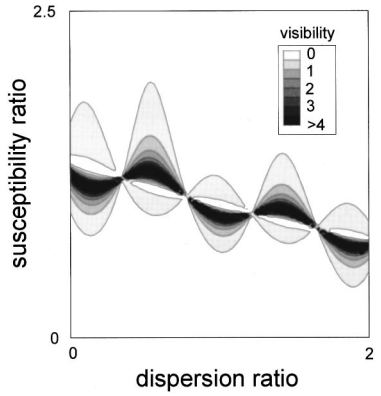

Fig. 9. Visibility of a stack consisting of 100 layers, each 0.5 μm thick, with focusing in the middle. Visibility is defined here as the absolute logarithm of the ratio between the yield for focusing on an interface to that for focusing halfway between the interfaces. The dispersion ratio is defined as $\Delta n_{\mathrm{gap}}/\Delta n_{\mathrm{glass}}$, where $\Delta n_{\mathrm{glass}} = -0.032$ and the susceptibility ratio is $\chi^{(3)}_{\mathrm{gap}}/\chi^{(3)}_{\mathrm{glass}}$.

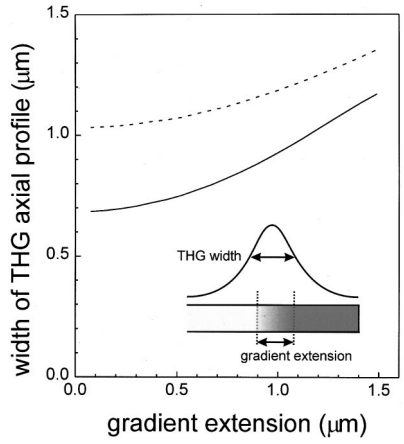

Fig. 10. Calculated gradient sensitivity (width of the THG axial profile at high NA) as a function of gradient extension between two different bulk materials. Two situations are displayed: Dashed curve, the materials have equal third-order susceptibility $[\chi^{(3)}_1 = \chi^{(3)}_2]$ but unequal dispersion ($\Delta n_1 = -0.022$ and $\Delta n_1 = -0.032$); solid curve, the two materials have equal dispersion ($\Delta n_1 = \Delta n_2 = -0.032$) but differ in third-order susceptibility $[\chi^{(3)}_1 = 4\chi^{(3)}_2]$.

We calculated the THG response of a gradient region by dividing that region into many homogeneous layers that contain mixtures of both pure materials, such that the amount of admixture increases linearly from one pure layer to the other (Fig. 10, inset). At every interface the required phase shift between the third-order material polarization and the induced THG beam has been accounted for. Any kind of spatial mixing profile between two materials can be simulated with this technique.

4. DISCUSSION AND CONCLUSIONS

The experiments and theoretical analysis have demonstrated the potential of THG microscopy for material characterization. In particular, double-interface geometry provides an excellent means for determining the ratios of the third-order susceptibilities of layer and substrate and also of their dispersion. Because of the coherent nature of the THG signal, interference effects show up in the THG axial profiles whose shapes depend markedly on the dispersion of the various media. One can effectively uncouple dispersion and susceptibility by measuring the axial profiles and THG conversion efficiencies, respectively. The functional shapes of the axial profiles are largely independent of the susceptibility ratio. The strongest dependence of the axial profiles on the material dispersion is achieved when the confocal parameter of the fundamental beam is equal to the distance between the interfaces. By characterizing the functional shapes of the axial profiles in terms of three ratios, and plotting these ratios as a function of NA, the comparison of experiment with theory allows for a straightforward determination of the dispersion. However, one can use the THG conversion efficiencies at high NA to determine the third-order susceptibility, because these efficiencies are practically insensitive to the dispersion of the materials involved.

The coherent nature of the THG process renders THG microscopy highly sensitive to the specific sample geometry. In general, various geometries may yield identical results and vice versa: Geometries that differ only slightly may yield widely different THG responses, as has become especially clear in our studies in the evaluation of the effect of periodic structures. Small differences in, for instance, either the thickness or the dispersion of the layers result in large differences in the THG response. This behavior is also clear from Fig. 9, which shows a strong dependence of the visibility of a particular periodic structure on both susceptibility and dispersion ratio. The message of this result is twofold: (i) It is virtually impossible to reconstruct the sample geometry and properties from complicated samples without any prior knowledge of the sample and (ii) with some *a priori* information about the sample, THG microscopy may provide detailed information on the various material parameters.

From theoretical arguments one expects paraxial theory to fail at high NA values, in which case other approximations (e.g., the Debye approximation) are more appropriate. At the highest NA values, even scalar diffraction theory is inadequate, and polarization effects

should be considered. However, we have found that all experiments are described adequately by the paraxial theory, even at high NA. A similar result was recently obtained by Potma *et al.*,[12] who concluded that the paraxial approximation underestimates the scalar diffraction theory results only slightly for high NAs in the case of coherent anti-Stokes Raman scattering microscopy. In this context it should be noted also that the famous classical description of the focal field at high-NA conditions with hat-profile pupil illumination in terms of the Lommel functions[9]—which has been verified experimentally in great detail—is actually based on two conflicting approximations, the Debye and the paraxial approximations.[13]

Finally, we note that THG microscopy can discriminate between interfaces composed of a sudden transition in material properties and those with a gradual change in these parameters when the confocal parameter of the fundamental beam is of the same order as or smaller than the physical extension of the gradient.

ACKNOWLEDGMENTS

This research was financially supported in part by the Stichting voor Fundamenteel Onderzoek der Materie, The Netherlands, under grant 94RG02, by the Stitchting Technische Wetenschappen, The Netherlands, under grant ABI.4929, and by BASF Aktiengesellschaft (Ludwigshafen, Germany). J. Squier acknowledges support from National Science Foundation grant DB1-9987257.

J. M. Schins's e-mail address is schins@science.uva.nl.

REFERENCES

1. J. F. Ward and G. H. C. New, "Optical third harmonic generation in gases by a focused laser beam," Phys. Rev. **185**, 57–72 (1969).
2. D. A. Kleinman, A. Ashkin, and G. D. Boyd, "Second-harmonic generation of light by focused laser beams," Phys. Rev. **145**, 338–379 (1966).
3. R. Eramo and M. Matera, "Third-harmonic generation in positively dispersive gases with a novel cell," Appl. Opt. **33**, 1691–1696 (1994).
4. A. Lago, G. Hilber, and R. Wallenstein, "Optical frequency conversion in gaseous media," Phys. Rev. A **36**, 3827–3836 (1987).
5. Y. Barad, H. Eisenberg, M. Horowitz, and Y. Silberberg, "Nonlinear scanning laser microscopy by third-harmonic generation," Appl. Phys. Lett. **70**, 922–924 (1997).
6. M. Müller, J. Squier, K. R. Wilson, and G. J. Brakenhoff, "3D-microscopy of transparent objects using third-harmonic generation," J. Microsc. (Oxford) **191**, 266–274 (1998).
7. J. Squier, K. R. Wilson, M. Müller, and G. J. Brakenhoff, "3D-microscopy using third-harmonic generation at interfaces in biological and non-biological specimens," in *Ultrafast Phenomena XI*, T. Elsasser, J. G. Fujimoto, D. Wiersma, and W. Zinth, eds., Vol. 63 of Springer Series in Chemical Physics (Springer-Verlag, Berlin, 1998), p. 153.
8. R. W. Boyd, *Nonlinear Optics* (Academic, Boston, Mass., 1992).
9. M. Born and E. Wolf, *Principles of Optics* (Pergamon, Oxford, 1980).
10. W. H. Press, W. T. Vetterling, S. A. Teukolsky, and B. R. Flannery, *Numerical Recipes in C* (Cambridge U. Press, Cambridge, 1992).
11. J. Squier, M. Müller, G. J. Brakenhoff, and K. R. Wilson, "Third harmonic generation microscopy," Opt. Express **3**, 315–324 (1998), http://www.opticsexpress.org.
12. E. O. Potma, W. P. de Boeij, and D. A. Wiersma, "Nonlinear coherent four-wave mixing in optical microscopy," J. Opt. Soc. Am. B **17**, 1678–1684 (2000).
13. J. J. Stamnes, *Waves in Focal Regions* (IOP Publishing, Bristol, UK, 1986).